ORIGINAL PAPER

Development of an ejector for passive hydrogen recirculation in PEM fuel cell systems by applying 2D CFD simulation

Gerald Singer[1] · Rebekka Köll[1] · Patrick Pertl[1] · Alexander Trattner[1,2]

Abstract

The anode subsystem is a major energy consumer of polymer-electrolyte-membrane (PEM) fuel cell systems. A passive hydrogen recirculation system, like an ejector, is an excellent solution to maximize hydrogen utilization while maintaining low parasitic losses. However, high development efforts are necessary to maximize the performance of the ejector for the entire operating range. This research paper provides part of a toolchain for ejector development, consisting in particular of a multi-parameter simulation based on rotational symmetric 2D CFD. The 2D CFD greatly helps optimize the design of the ejector, reducing development effort, and increasing accuracy. In addition, the main correlations between thermodynamic states and geometry on the entrainment ratio are evaluated. Subsequently, an ejector is designed for a PEM fuel cell application using 2D CFD and the results show in which operating range a single ejector can be applied. This toolchain enables rapid design and optimization of ejector geometry, saving development time and cost while increasing accuracy and extending the operating range.

Keywords PEM fuel cell · Passive anode hydrogen recirculation · Ejector development toolchain · Rotational symmetric 2D CFD · Multi-parameter simulation · Design of experiment DoE

List of symbols

Latin letters

A_i	Area at position i [m^2]
c_i	Velocity of mass flow i [m/s]
c_p	Specific heat capacity [J/(kg K)]
d_i	Diameter of i [mm]
F	Faraday's constant $= 96{,}485$ [As/mol]
I	Fuel cell current [A]
k	Kilo $= 10^3$ [−]
l_i	Length of i [mm]
M	Mach number [−]
M_i	Molar mass of species I [g/mol]
N	Number of cells [−]
$\dot{m}_i$	Mass flow at position i [g/s]
p_i	Pressure at position i [Pa]
R_i	Gas constant for gas i [kJ/kg K]
T_i	Temperature at position i [K]
z	Valency, number of electrons per mol in reaction [−]

Greek letters

Δ	Difference
θ	Angle of diffuser [°]
κ	Isentropic exponent [−]
λ	Hydrogen stoichiometric ratio [−]
μ_i	Mass fraction of species i [−]
ρ_i	Density at position i [kg/m^3]
ψ_{max}	Flow coefficient at critical condition [−]
ω	Entrainment ratio [−]

Subscripts and superscripts

avg	Average
b	Back
crit	Critical
d	Discharge
diff	Diffuser
eje	Ejector
in	Inlet
FC	Fuel cell
H$_2$	Hydrogen

✉ Gerald Singer
  singer@hycenta.at

1   HyCentA Research GmbH, Inffeldgasse 15, 8010 Graz, Austria

2   Institute of Thermodynamics and Sustainable Propulsion Systems, Graz University of Technology, Inffeldgasse 19, 8010 Graz, Austria

max	Maximum
min	Minimum
mix	Mixing chamber; mixing
out	Outlet
prim	Primary
sec	Secondary
t	Nozzle throat@@

Abbreviations

1D, 2D, 3D	One, two and three spatial dimensions
BoP	Balance of plant
CFN	Critical flow nozzle
DoE	Design of experiments
FC	Fuel cell
MEA	Membrane electrode assembly
NXP	Nozzle exit position
OCV	Open-circuit voltage
PEM	Polymer electrolyte membrane or proton exchange membrane
PFSA	Perfluorosulfonic acid
Re	Reynolds number
SIM	Simulation
TS	Timeshare

1 Introduction

Greenhouse gases are present in the Earth's atmosphere and trap heat from the sun, increasing the Earth's surface temperature. The amount of greenhouse gases in the atmosphere has increased as a result of human activities like the burning of fossil fuels and deforestation. Using hydrogen as a fuel is one major way to reduce greenhouse gas emissions [1]. PEM electrolysis, a process that uses electricity to convert water into hydrogen and oxygen, can be used to produce hydrogen. When electrolysis is performed with renewable energy, hydrogen can be used as a clean and effective fuel. One application of using hydrogen is by converting the hydrogen back to electricity in PEM fuel cell systems [2]. Since only water is produced when hydrogen is used in fuel cells, it is a cleaner energy source than fossil fuels and can help solve the climate crisis. PEM fuel cell applications in mobility made great development progress in recent years through improvements at the system, subsystem, and component levels [3–16]. However, further improvements are necessary for increasing the attractivity of fuel cell electric vehicles and stationary applications by reducing development time and costs.

The main component of a PEM fuel cell system is the fuel cell stack which consists of several cells. As the hydrogen is consumed at the active area in the PEM fuel cell, the hydrogen partial pressure at the anode decreases, resulting in a lower hydrogen availability at the anode flow field outlet.

Therefore, more hydrogen needs to be supplied than the fuel cell uses to guarantee that the complete active area receives sufficient hydrogen and maintains a high fuel cell voltage. However, excessive hydrogen needs to be recirculated to maximize hydrogen utilization. The recirculation can either be carried out actively by means of a hydrogen blower or passively by means of an ejector.

The ejector performance highly depends on the geometry and the operating conditions at inlets and outlets. Based on previous work [17], a further toolchain method can be introduced for maximizing performance and accelerating the development of ejectors in PEM fuel cell applications. The development toolchain can be extended by a 2D CFD simulation, in which the ejector flow field is optimized by a rotational symmetric model and design of experiment (DoE) approach (Fig. 1). The main advantage of 2D CFD is that the ejector performance can be predicted faster due to the low computational cost. Moreover, by applying a suitable automated DoE method, a high number of simulation runs can be performed, and the accuracy of the result can be optimized by selecting a suitable cell size.

A preliminary simulation analysis of the ejector has been mainly conducted via the following two simulation strategies:

- Modeling of the ejector by a zero- (0D) or a one-dimensional (1D) simulation model [18–21].
- Application of a commercially available CFD software for two-dimensional (2D) or three-dimensional (3D) simulations.

The difference between the 0D, 1D, 2D, or 3D simulation is the discretization in space. The lower the degree of freedom, the lower the complexity and typically less computational effort is necessary. However, for complex ejector flow field analyses with geometric influences, a 2D CFD model provides more details compared to a 1D model. A 3D CFD
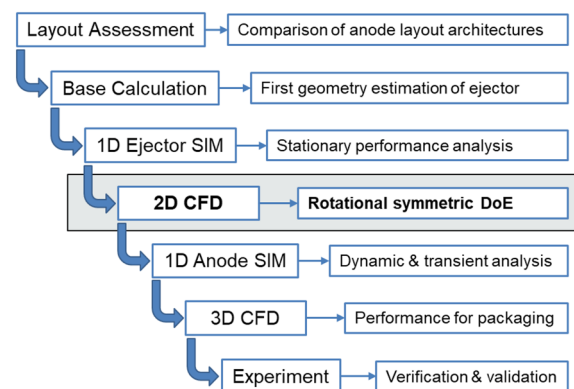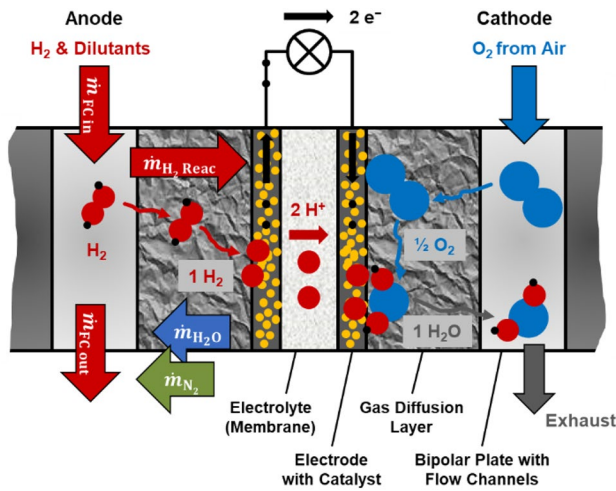

Fig. 1 Toolchain: methods and results ([17], adapted)

Table 1 Applied 2D and 3D CFD turbulence models for PEM fuel cell applications

Turbulence model	Source
k-ε standard, RNG, or realizable	[23–26]
k-ω SST	[22, 27–30]

Fig. 2 Schematic PEM fuel cell (adapted [2])

model provides even more details regarding non-rotational symmetric influences, such as inlet and outlet piping, but the 2D CFD has less computational costs. For example, considering only the rotational symmetric part, if the 3D CFD simulation has 1 cell per degree angle, the 3D CFD model has a 360 times larger mesh than the 2D CFD model, which significantly increases the simulation time.

Table 1 states the most common applied turbulence models for 2D and 3D CFD simulation in the literature for ejectors in PEM fuel cell applications. Large-Eddy simulations are not considered for supersonic ejectors due to the high Reynolds numbers [22].

Before the 2D CFD simulation methodology for a rotational symmetric ejector model is presented in this work, the general boundary conditions of a fuel cell stack have to be analyzed.

1.1 PEM fuel cell

The fuel cell consists of the membrane electrode assembly (MEA) which characterizes the electrochemical performance and the bipolar plates which are responsible for the hydrogen and oxygen supply (Fig. 2). The MEA contains the membrane, the catalyst layer on a carbon support layer, and the gas diffusion layer (GDL).

The membrane typically consists of PFSA ionomer (perfluorosulfonic acid). The membrane has a water uptake capability that enables proton conductivity. The membrane resistance is therefore dependent on the humidity of the membrane and also on its thickness, whereas the membrane thickness greatly influences its mechanical stability [31–33].

The electrodes are highly porous, enabling the delivery of hydrogen and air, electrically conductive, and are in contact with the membrane material. The interface of reactant gas, proton conductive material, and electrically conductive reaction catalyst creates the triple-phase boundary, where the electrochemical reactions take place at the catalyst surface. At the anode, hydrogen is reduced to protons, that pass the membrane to the anode. The dominant proton transport mechanism in sulfonated PFSA membranes is a fast proton hopping from one hydronium ion to the next, described as Grotthuß diffusion [34–36]. At the cathode, the protons are consumed by the formation of water with reduced oxygen. Due to the electrically isolating membrane, the electrons produced at the anode are forced to flow through a circuit, producing an electric current, and subsequently to the cathode, enabling the reduction of oxygen [37, 38].

The bipolar plate provides the required hydrogen or oxygen flow (air) channels and is the main component responsible for the total height of a fuel cell stack. The design and height of the flow channels have a great influence on the media distribution and the pressure drop in the flow field. The gas diffusion layer (GDL) provides an even distribution of flow reactants to the triple-phase boundary layer [39–43].

The hydrogen pressure loss across the inlet and outlet of the bipolar plate is critical for the ejector performance. One fuel cell produces only a limited power output based on the maximum current density and the active area. Therefore, fuel cells are stacked to increase the total power output [44].

1.2 Hydrogen supply

Hydrogen and humidity, as well as impurities, are supplied by the anode inlet ($\dot{m}_{\text{FC in}}$, Fig. 2). As the hydrogen gas flows over the anode, the hydrogen passes through the gas diffusion layer and reacts at the triple-phase boundary ($\dot{m}_{\text{H}_2\text{ Reac}}$).

The theoretical hydrogen consumption by water formation m of a PEM fuel cell is calculated by Faradays law ($\dot{m}_{\text{H}_2\text{ Reac}}$, Eq. 1). m is directly proportional to the current I and the numbers of cells N. Since oxygen is reduced from oxidation state 0 to −II, the valency z is 2 (Fig. 3).

Equation 1: Faraday's law [45]

$$\dot{m}_{\text{H}_2\text{ Reac}} = \frac{I \bullet M_{H_2} \bullet N}{z \bullet F}. \tag{1}$$

In practice, more hydrogen than the theoretical amount consumed by the reaction is supplied to the fuel cell stack
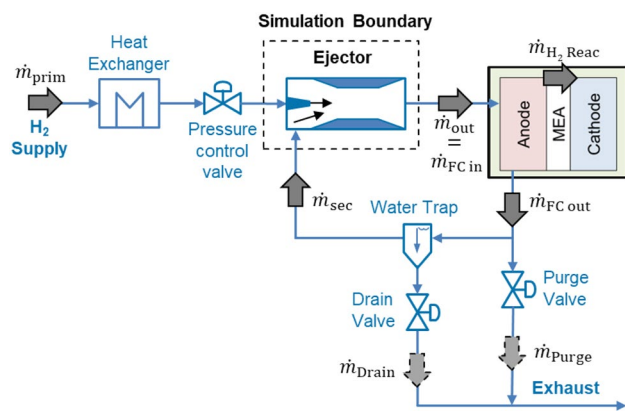
Fig. 3 Ejector simulation boundary (adapted [17])

to strictly avoid fuel starvation at the anode catalyst caused by diffusion limitation, delay in hydrogen delivery, pinholes, and competing reactions consuming hydrogen. The ratio between available hydrogen and reacted hydrogen is the stoichiometric ratio λ.

Equation 2: Hydrogen stoichiometric ratio

$$\lambda = \frac{\dot{m}_{H_2 \, FC \, in}}{\dot{m}_{H_2 \, Reac}}. \tag{2}$$

The higher stoichiometric ratio means that not all of the hydrogen provided is utilized in the fuel cell. Recirculation is required to recover the excess hydrogen and minimize hydrogen losses.

Dead-end mode operation does not recirculate hydrogen and is not considered in this work because of the higher hydrogen consumption, lower cell voltages, and higher degradation rates compared to recirculation systems [46, 47].

Due to the thin membrane and concentration differences, water back diffusion ($\dot{m}_{H_2O}$) and nitrogen crossover ($\dot{m}_{N_2}$) accumulate and reduce the hydrogen concentration in the fuel cell due to hydrogen recirculation. Therefore, a purge cycle for removing the nitrogen (and gaseous water) is necessary after a certain period to increase the hydrogen concentration and prevent a voltage drop or fuel starvation. Purge cycles result in hydrogen losses, and therefore, a well-designed purge strategy can increase hydrogen utilization while maintaining high cell voltages [48–50].

Liquid water is separated into a water trap in the anode recirculation system and drained periodically. A certain amount of water-level content in the membrane is necessary to keep ionic conductivity high and prevent membrane dry-out (ohmic losses). Generally, the water is produced on the cathode side and humidifies the membrane. However, too much liquid water leads to flooding in the anode and partially blocking the active area [51–54].

To discharge the liquid water from the stack, a higher pressure drop of the fuel cell stack is assumed and the recirculation is designed slightly higher. In case the fuel cell is not supplied with sufficient hydrogen, fuel starvation occurs, the cell voltage decreases locally, and the fuel cell degrades [55, 56].

1.3 Degradation caused by hydrogen fuel starvation

A shortage of fuel in the cell not only causes a power drop, but also causes serious degradation of the catalyst layer. The main degradation mechanism occurring in the fuel cell due to fuel starvation is the electrochemical carbon corrosion. Two degradation mechanisms can occur [57–60]:

- Carbon corrosion on the cathode side appears at high cathodic potentials (>0.8 V) due to a partial/local hydrogen starvation.
- Carbon corrosion on the anode side due to complete hydrogen starvation.

Carbon corrosion is possible due to the presence of platinum at the anode and cathode which lowers the oxidation resistance of carbon. The carbon reacts to CO_2 at the interface between the platinum and the carbon support layer (Eq. 3). As a result, there is a loss of contact between the platinum and the carbon support layer, followed by decreased catalytic activity and higher activation overvoltages. Additionally, electrode thinning could occur resulting in increased ohmic resistances.

Fuel starvation not only causes a power drop but irreversible degradation of the carbon material in the stack, primarily of the catalyst support. Carbon is not thermodynamically stable at potentials higher than 0.207 V (Eq. 3), but is kinetically inert up to higher potentials, enabling its usage in PEM fuel cells. At very high electrode potentials, carbon corrosion can occur at both electrodes.

The carbon material at the cathode can be oxidized at partial fuel starvation with an in-plane electron transfer, where the cathodic potential is forced to very high values. The carbon material at the anode side is caused by a complete fuel starvation, forcing the anode to produce protons by water splitting and consequently carbon oxidation.

As a consequence, the active area of the triple-phase boundary decreases due to the loss of conductive material, loss of pore structure, and loss of contact with the catalyst and the membrane material. Therefore, a sufficient hydrogen stoichiometry has to be ensured by the hydrogen recirculation system.

Equation 3: Carbon corrosion in PEM FC

Table 2 Comparison overview ejector and blower

Criteria	Ejector	Blower
Number of components and moving parts	Low +	High –
Weight and volume	Low +	High –
Energy demand	Low +	High –
Production cost	Low +	High –
Setting possibility of the recirculated mass flow	Low –	High +

+ = favorable, – = unfavorable

$$C + 2H_2O \rightarrow CO_2 + 4H^+ + 4e^- E_0 = 0.207V. \tag{3}$$
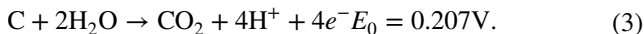
As a result, the main underlying influencing factor for carbon corrosion is a low hydrogen stoichiometry caused by insufficient hydrogen supply at the anode inlet. Therefore, sufficient hydrogen stoichiometry has to be ensured to mitigate carbon corrosion by the hydrogen recirculation system [61].

1.4 H$_2$ recirculation

The recirculation can either be carried out actively by means of a hydrogen blower or passively by means of an ejector (Table 2) [17].

Ejectors are generally more compact and reliable than recirculation blowers, because the ejector is a relatively simple component with no moving parts [20]. Additionally, no energy demand is required for operating an ejector except for a pressure regulator [62]. A typical recirculation blower consumes between 400 W and up to 2 kW for automotive applications [63, 64]. In comparison, a pressure control valve typically has less than 20 W, which is necessary for both active and passive recirculation. The recirculation blower has higher weights, and higher costs in production and issues can arise due to corrosion [65].

However, the recirculation blower can provide the appropriate hydrogen mass flow to the fuel cell over a wide range of load points, ensuring that the fuel cell is supplied with the necessary hydrogen under all operating conditions. The ejector's recirculated mass flow is defined by the geometry and by the thermodynamic states at inlets and outlets. Therefore, the recirculated mass flow needs to be designed specifically for the application and, hence, the setting possibilities of the recirculated mass flow are limited. To guarantee the same reliable hydrogen supply with the ejector but with all other previously mentioned advantages, the ejector flow field needs to be simulated and optimized over the entire operating range.

The main components of the anode path and the ejector with its simulation boundary are illustrated in Fig. 3. The ejector outlet pressure p_{out} is the fuel cell anode inlet
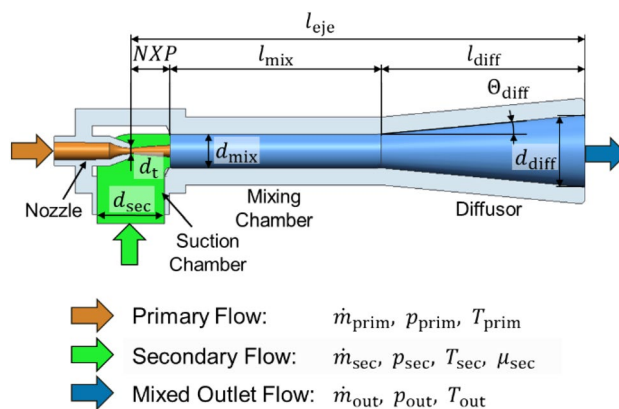
Fig. 4 Ejector main geometry (adapted [17])

pressure and the secondary inlet pressure p_{sec} is the fuel cell anode outlet including the water trap.

The ejector has a primary flow, a secondary flow, and an outlet flow (Fig. 4). The ejector consists of two main investigation areas, the nozzle and the rest of the ejector consisting of a suction chamber, a mixing chamber, and a diffuser.

The nozzle is responsible for the maximum possible hydrogen mass flow supply and the minimum possible hydrogen supply at critical conditions (a sonic condition in the nozzle throat). The suction chamber, mixing chamber, and diffuser define the performance of the ejector.

1.4.1 Nozzle

The hydrogen mass flow control through the nozzle can be applied by the nozzle inlet pressure-based control (pulsed or continuous pressure) or the nozzle throat area control (needle or multi-pipe approach) and combinations of previously named [17]. Additional hydrogen mass flow control applications can be reviewed in [66–71].

The hydrogen mass flow through a nozzle is calculated by the nozzle throat area A_t, nozzle inlet pressure p_{prim} and temperature T_{prim}, the critical flow coefficient $\psi_{crit\,H_2}$, and the discharge coefficient c_d (Eq. 4). Each parameter and its influences are analyzed below.

Equation 4: Nozzle hydrogen mass flow

$$\dot{m}_{prim} = A_t \bullet p_{prim} \bullet \sqrt{\frac{2}{R_{H_2} \bullet T_{prim}}} \bullet \psi_{crit\,H_2} \bullet c_d$$

$$A_t = \frac{d_t^2 \bullet \pi}{4}. \tag{4}$$

Generally, the lower the nozzle throat diameter, the higher the performance of the ejector. However, with decreasing

diameter, the nozzle inlet pressure increases quadratic ($d_t^2 \sim p_{prim}$) [23, 72].

The nozzle inlet temperature depends on the initial temperature of the hydrogen in the storage system and on whether a hydrogen heat exchanger is connected upstream to the nozzle. Typically, a hydrogen heat exchanger is used and the hydrogen at the nozzle inlet has a temperature of 60–70 °C. A higher nozzle inlet temperature also results in a higher mixed gas temperature at the inlet to the fuel cell stack, and no condensation of water can occur (flooding).

The critical flow coefficient for hydrogen $\psi_{crit\,H_2}$ depends on the isentropic exponent (Eq. 5), which depends on temperature and pressure at the nozzle throat. The critical pressure and temperature are calculated by an isentropic change of state at nozzle inlet conditions. The critical flow coefficient is calculated by real gas data based on REFPROP [73] and displayed in Fig. 5.

Equation 5: Critical states and flow coefficient for hydrogen

$$p_{crit} = \left(\frac{2}{\kappa + 1} \right)^{\frac{\kappa}{\kappa - 1}} \bullet p_{prim}$$

$$T_{crit} = \frac{2}{\kappa + 1} \bullet T_{prim}$$

$$\psi_{critH_2} = \sqrt{\frac{\kappa}{\kappa + 1}} \bullet \left(\frac{2}{\kappa + 1} \right)^{\frac{1}{\kappa - 1}}. \tag{5}$$

The critical flow coefficient has a higher dependency on the temperature than on the pressure. The critical flow coefficient influences the total hydrogen mass flow of $< 0.5\%$.

In Eq. 4, the discharge coefficient c_d describes the real mass flow through a nozzle compared to an isentropic nozzle and, therefore, takes the nozzle geometry into account. The discharge coefficient can be expressed as a function of the Reynolds number (Re) [74–78]. A typical hydrogen nozzle for a fuel cell appli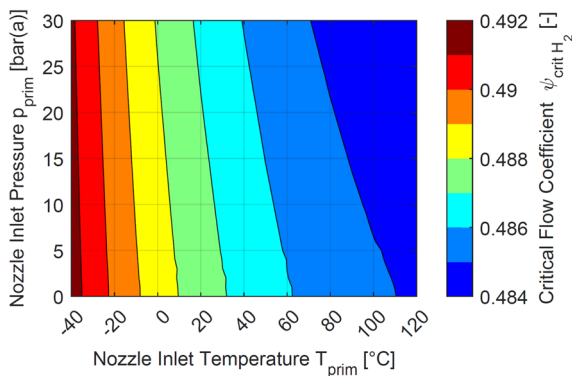cation between 30 and 200 kW has a throat diameter d_t between 1 and 3 mm. A Reynolds number range is given in Eq. 6 for typical PEM fuel cell conditions in vehicle applications (nozzle inlet: 3–30 bar(a) and 70 °C).

Equation 6: Reynolds number range hydrogen nozzle

$$Re = \frac{c_{crit} \bullet d_t}{v_{crit}} = 4 \bullet 10^4 \text{ to } 10^6. \tag{6}$$

Figure 6 shows two possible nozzle geometries for critical flow throat (CFN) design. The continuous line shows the area for a relative uncertainty of 0.3% with a 95% confidence interval. Both CFNs decrease quickly to lower Reynold values due to the increased friction loss near wall. The discharge coefficient is highly similar comparing hydrogen with nitrogen for Reynolds numbers > 1000 [79], because they have a similar value of isentropic exponent. Both hydrogen and nitrogen are diatomic molecules.

Reynolds number range for typical PEM fuel cell ejectors indicates that the nozzle throat operates mainly in the laminar region. Neglecting the influences of the discharge coefficient can result in a real hydrogen mass flow deviation of up to 4%.

The discharge coefficient and the critical flow coefficient must be taken into account to determine the diameter of the nozzle throat and thus the maximum possible hydrogen supply. In addition, purging, draining, and a certain transient load change safety margin should be considered as well.

1.4.2 Suction chamber, mixing chamber, and diffuser

For the performance of the ejector, the suction chamber, the mixing chamber, and the diffuser are responsible.

The suction chamber is responsible for optimal secondary intake flow. Typically, the secondary mass flow enters
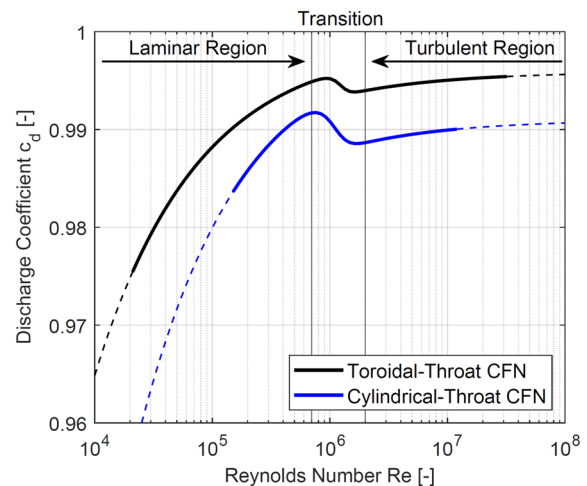

Fig. 5 Critical flow coefficient ψ_{critH_2} based on real gas data

Fig. 6 Discharge coefficient c_d dependent on turbulence regime and nozzle geometry [77]

on one side of an ejector system. Therefore, non-symmetric flow occurs and may deflect the primary nozzle flow, which decreases performance. If the ejector packaging allows, a rotational symmetric suction chamber is favorable with high secondary inlet cross sections to reduce the incoming velocity. Since a 2D CFD model requires a rotational symmetric axis, the suction chamber must be analyzed in the 3D CFD simulation (Fig. 1). Experience has shown that a minimal suction chamber inlet diameter d_{sec} of 20 mm is recommended for fuel cell vehicle applications.

The mixing chamber and diffuser should be highly concentric to the nozzle axis. Often packaging requirements limit the maximum length of the ejector l_{eje}. The mixing chamber length and the diffuser length share the maximum available ejector length, since the nozzle and NXP can often be made relatively short. The diffuser outlet should be chosen as big as possible to minimize pressure losses between the ejector outlet and fuel cell stack inlet.

Recommended parameter range [23, 24]:

- Nozzle exit position: $NXP = 0$–$4 \cdot d_{\text{t}}$
- Mixing chamber diameter $d_{\text{mix}} = 2$–$6 \cdot d_{\text{t}}$.

2 Methodology

First, the boundary conditions of the ejector are described. Then, the trade-off between mesh size, accuracy, and simulation time is explained. Finally, a general optimization study of the entrainment ratio provides details about how to maximize performance. The ejector secondary mass flow is used to calculate the entrainment ratio ω of the ejector and further the stoichiometric ration λ of the fuel cell. Those are the key performance indicators. The following equations are valid for steady-state conditions [17].

Equation 7: Entrainment ratio ω and stoichiometric ratio λ

$$\omega = \frac{\dot{m}_{\text{sec}}}{\dot{m}_{\text{prim}}}$$

$$\lambda = 1 + \mu_{\text{sec H}_2} \bullet \omega. \tag{7}$$

Generally, the entrainment ratio needs to be maximized, which also maximizes the stoichiometric ratio. Thermodynamic states as well as geometries can be varied to maximize the entrainment ratio.

2.1 System-level boundary conditions

Many parameters can be defined before starting the simulation optimization due to the boundary conditions of the anode path. The following boundary conditions are typically given for the hydrogen recirculation system.

Fuel cell stack boundary conditions:

- The fuel cell power request requires a certain hydrogen mass supply through the ejector's nozzle. And the nozzle inlet pressure p_{prim} is defined by the hydrogen mass flow.
- The fuel cell inlet pressure and the pressure loss over the stack are given for a certain operating condition by the fuel cell stack manufacturer.
- Water separation efficiency is assumed to be 100% (due to very high separation efficiencies achieved in a previous analysis [80–82]).

Ejector boundary conditions:

- Nozzle throat diameter d_{t} should be as small as possible, respecting the maximum available nozzle inlet pressure to maximize performance.
- The diffuser outlet diameter is maximized to the available diameter of the anode FC inlet.
- Ejector length l_{eje} is limited according to packaging requirements.

The following parameters are variable according to the preliminary stated boundary conditions:
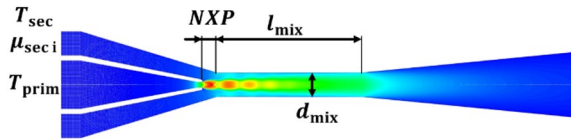
Variable parameters:

- Geometry:

    o   Nozzle exit position: NXP
    p   Mixing chamber length l_{mix}
    q   Mixing chamber diameter d_{mix}

- Thermodynamic states:

    o   Primary inlet temperature T_{prim}
    p   Secondary inlet temperature T_{sec}

- Secondary inlet mass concentration: $\mu_{\text{sec i}}$

    o   Hydrogen $\mu_{\text{sec H}_2}$
    p   Nitrogen $\mu_{\text{sec N}_2}$
    q   Water $\mu_{\text{sec H}_2\text{O}}$.

This leads to a multi-parameter CFD simulation system of seven degrees of freedom for a given fuel cell stack load point (Fig. 7). The secondary inlet concentration has two degrees (instead of three), because the third concentration can be calculated according to Eq. 8.

Equation 8: Secondary mass concentration

$$1 = \mu_{\text{sec H}_2} + \mu_{\text{sec N}_2} + \mu_{\text{sec H}_2\text{O}}. \tag{8}$$

Fig. 7 Exemplary ejector 2D CFD velocity flow field with the six variable parameters

To simulate the multi-parameter model, the following simulation model setup is used (Table 3).

A mesh size analysis is conducted with the previously stated simulation setup.

2.2 Mesh analysis, and trade-off between simulation time and accuracy

The mesh size has a significant influence on the simulation time and accuracy. Figure 8 shows the influence on the velocity stream between a mesh size of 20 k, 75 k, 170 k, and 4000 k cells for the same boundary condition. The Mach diamonds are hardly visible for a 20 k mesh size compared to 4000 k.

The Mach diamonds result from the expansion of the nozzle flow into the suction chamber which results in supersonic velocities above 2000 m/s. A difference between the 20 k and 4000 k is that the high gradients of the diamonds are visible with a higher resolution. The higher the mesh size, the higher the velocity which also enhances the entrainment ratio.

Figure 9 compares different mesh sizes and the resulting entrainment ratio and evaluates four of these meshes in detail. The entrainment ratio does not change significantly for very high mesh sizes (> 1000 k). A mesh size of 200 k cells has less than a 1% deviation compared to an "infinite" mesh size. Furthermore, a low mesh size is rather a conservative result compared to a high mesh size. If for example, the cell count is too high (200 k instead of
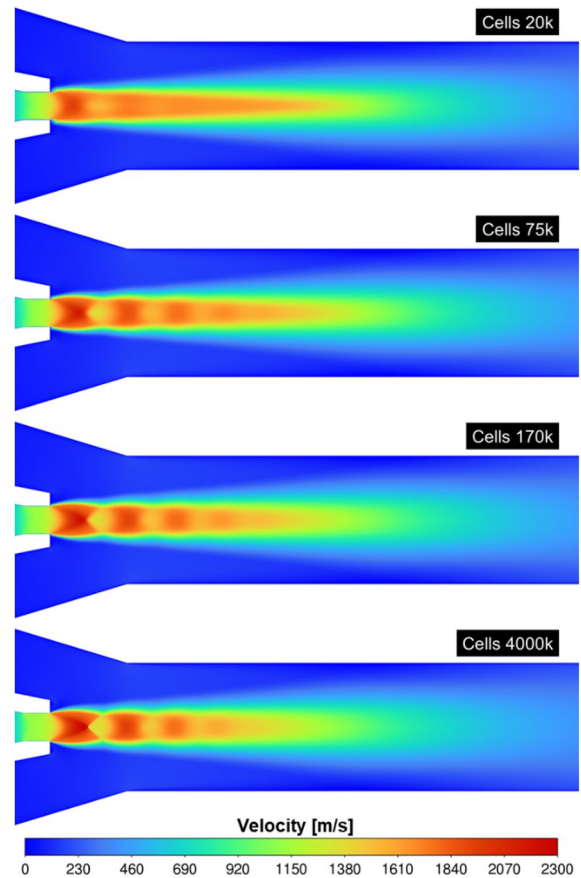
Fig. 8 Ejector mesh size influence

80 k), then approximately three times as many simulations can be conducted or the total amount of simulation time can be reduced by approximately 67% while maintaining high accuracy with < 2% deviation.

The simulations are performed on a standard computer (specifications in Table 4). The time durations for the simulations are specified in Fig. 9.

Table 3 2D rotational symmetric CFD setup

| Simulation tool	Ansys fluent
Turbulence model and setup	k-ε model realizable
	Enhanced wall treatment
	Viscous heating
	Compressibility effects
Material	Ideal gas; ideal-gas-mixing-law
Model interfaces	Primary inlet: mass flow inlet with temperature
	Secondary inlet: pressure inlet with temperature, H_2, N_2 and H_2O concentration
	Ejector outlet: pressure outlet
Mesh	20–4000 k cells, quadrilateral cells
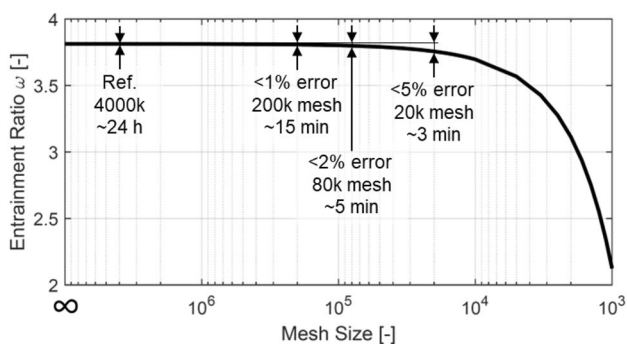
Fig. 9 Trade-off: mesh size, accuracy, and simulation time

Table 4 Computer setup

CPU	Intel(R) Core(TM) i5-8500
	3.00 GHz up to 4.10 GHz
	6 cores (4 cores allocated for CFD)
RAM	32 GB, DDR4 SDRAM, 2666 MHz

If the same 2D CFD simulation is performed with a 3D CFD model with a cell angle of 3°, the mesh size increases by a factor of 120. This leads to a mesh size of 10 million cells considering a 2D CFD mesh size of 80 k cells. DoE optimization with a mesh size of 10 million is very computationally intensive and is therefore not recommended.

Therefore, the ejector geometry should be developed with 2D CFD instead of 3D CFD due to the high computational effort. In addition, to further minimize the simulation effort, the piping connections to and from the fuel cell and the ejector should be simulated separately by a 3D CFD model. After minimizing the pressure of the piping, the complete 3D CFD should be simulated for validation purposes only.

Depending on the level of result accuracy and number of simulation points, the mesh size is adjusted.

2.3 Sensitivity analysis of entrainment ratio

Due to the large number of variable parameters that influence each other, ejector development usually requires many simulations to optimize the performance range. Table 5 shows the parameter variation range for the following simulations. The following figures are displayed with the constant values.

Depending on the number of variable parameters, a strategy for the number of different simulations is required. If a seven-parameter Design of Experiments (DoE) is performed with a full factorial design, the number of simulations for ten variations of each parameter is 10 million, which is neither feasible nor needed. Therefore, the number of simulations should be decreased using sampling techniques. Examples

Table 5 Parameter variation range and constant value

Parameter	Min	Const	Max
d_{mix} [mm]	3	4.3	8
NXP [mm]	0	4	10
l_{mix} [mm]	10	17	30
T_{prim} [K]	273	293	353
T_{sec} [K]	273	343	373
p_{sec} [bar(a)]	1.15	1.18	1.25
p_{out} [bar(a)]	1.30	1.38	1.45
$\mu_{sec\,H_2}$ [%]	0	24	100
$\mu_{sec\,N_2}$ [%]	0	46	50
$\mu_{sec\,H_2O}$ [%]	0	30	50

of DoE sampling designs include Latin Hypercube Sampling Design, Central Composition Design (CCD), or Optimal Space-Filling Design (OSF).

Figure 10 illustrates the entrainment ratio map, which was generated from the 2D CFD simulation results (Latin Hypercube Sampling Design) using the genetic aggregation surface methodology type. The constant values of Table 5 are used for the following figures.

Based on Fig. 10, the mixing chamber diameter has a higher influence on the entrainment ratio compared to the nozzle exit position and mixing chamber length. Since the axis of the entrainment ratio has the same scale, it can be seen that the mixing chamber length has a slightly greater influence than the nozzle exit position. A minimum mixing chamber length is necessary for the exchange of momentum between the primary mass flow and secondary mass flow (blue curve, $l_{mix} = 10\,mm$, Fig. 10).

Figure 11 shows the influence on the entrainment ratio over the primary temperature T_{prim} and secondary temperature T_{sec}. The entrainment ratio increases at higher primary temperatures, indicating that the use of a hydrogen heat exchanger upstream of the nozzle inlet is recommended. The entrainment ratio also increases with lower secondary temperatures, due to higher suction density.

Increasing the primary temperature T_{prim} leads to higher sonic velocities in the nozzle throat, which further increases the impulse of the gas flow and, thus, the higher the entrainment ratio of the ejector (Eq. 9).

Equation 9: Sonic velocity of hydrogen c_{crit}

$$c_{crit} = \sqrt{\kappa \cdot R_{H_2} \cdot T_{crit}}. \tag{9}$$

A heat exchanger between the fuel cell anode outlet and the hydrogen nozzle inlet is advantageous. The reduced temperature at the anode outlet increases the nozzle inlet temperature. As it can be seen in Fig. 11, both the lower temperature of the secondary gas and the increased temperature of the nozzle inlet enhance the entrainment ratio.
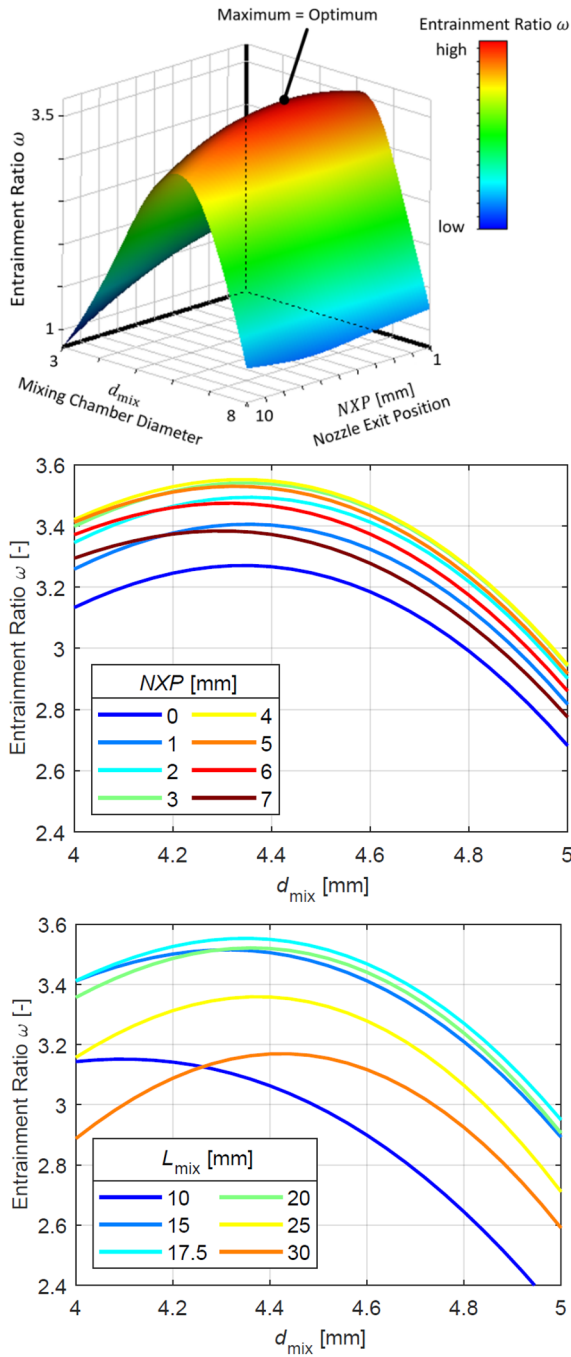
Fig. 11 Temperature sensitivity

Fig. 10 Geometry correlation on entrainment ratio
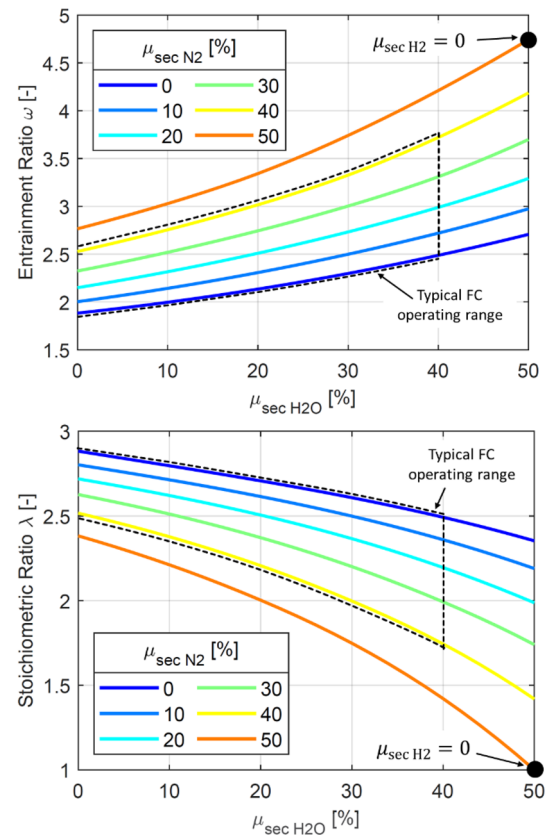
Fig. 12 Secondary mass concentration sensitivity

The entrainment ratio increases with higher concentrations of nitrogen and water due to the increased molar mass of the mixed gas (Fig. 12). However, even though the entrainment ratio increases, the stoichiometric ratio decreases. The highest stoichiometric ratio can be achieved with 100% hydrogen concentration at the secondary inlet. Typical stoichiometric ratios are between 1.4 at full load and can be as high as 5 at part load.

Figure 13 shows the influence on the sensitivity of the pressures between the secondary inlet and the ejector outlet. These pressures are defined by the system, but additional components in the anode recirculation can introduce additional pressure losses leading to reduced entrainment
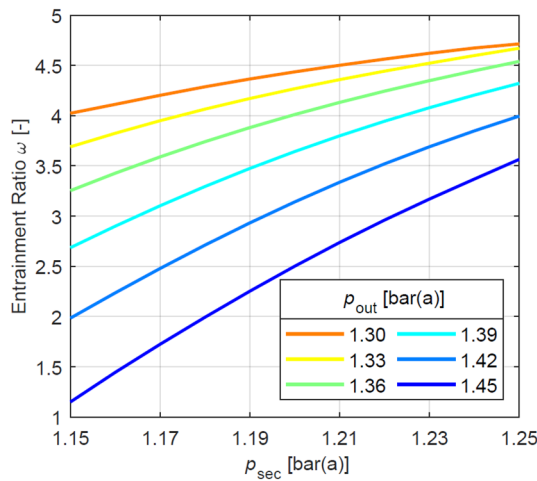
Fig. 13 Pressure sensitivity

ratios. With an additional pressure loss of 0.15 bar, the entrainment ratio can vary up to a factor of 3. As a result, additional pressure loss between stack inlet and outlet has the highest influence on entrainment ratio.

The entrainment ratio dependencies on geometries and thermodynamic states are in line with the literature [21, 83, 84]. The next step describes the results of a single ejector considering FC-specific boundary conditions.

3 PEM FC ejector optimization and operating strategy

In this chapter, an ejector for a PEM fuel cell application is designed considering the appropriate boundary conditions.

3.1 Boundary conditions specific fuel cell system

The following boundary conditions are given for the specific PEM fuel cell stack, which need to be satisfied by the ejector application (Table 6). The fuel cell stack's nominal power rating is 30 kW. The minimum stoichiometric ratio required from the fuel cell increases for lower loads.

Furthermore, the following boundary conditions are given on the anode level.

Boundary conditions:

- Maximum nozzle inlet primary pressure $p_{\text{prim max}} = 12$ bar(a)
- An anode heat exchanger is available to adjust the hydrogen temperature. Primary temperature $T_{\text{prim}} = 70°C$
- Secondary temperature $T_{\text{sec}} = 70°C$
- Maximum ejector length $l_{\text{eje}} = 120$ mm.

For the development of the optimized ejector, the following geometric parameters are available for optimization at each load point:

- Mixing chamber diameter d_{mix}
- Nozzle exit position: *NXP*
- Mixing chamber length l_{mix}.

3.2 Ejector design

During PEM fuel cell operation, the fuel cell operates at different load conditions, and hence, the thermodynamic states of the ejector change and thus the optimal geometry change. The local optima are simulated by the minimum hydrogen mass concentration $\mu_{\text{sec H}_2\text{min}}$ stated in Table 6, which represents the worst-case stoichiometric ratio. The best-case stoichiometric ratio is 100% hydrogen at the secondary inlet. If the hydrogen concentration falls below the minimum, a purge cycle is required to increase the hydrogen concentration.

Figure 14 shows the ejector entrainment ratio maps for four different load conditions stated in Table 6 at each optimized mixing chamber length (similar to Fig. 10 top). The load point (11%) does not achieve the defined minimum stoichiometric ratio of 5 due to the high-pressure difference between the anode FC inlet and outlet and the high required stoichiometric ratio according to boundary conditions.

Each load point has an optimum for the ejector geometry to maximize the entrainment ratio and the stoichiometric ratio. The local optimum stoichiometric ratio $\lambda_{\text{local opt}}$ is calculated by the maximum entrainment ratio according to Eq. 7 (Table 7). If the load point, which corresponds to the nozzle hydrogen mass flow, of the PEM FC stack decreases, then the optimum of the NXP, and mixing chamber diameter and length decrease as well.

The local optimum stoichiometric ratio $\lambda_{\text{local opt}}$ and the minimum stoichiometric ratio λ_{min} are displayed in Fig. 15.

Table 6 Fuel cell stack boundary conditions

Load [%]	$\dot{m}_{\text{prim}}$ [g/s]	λ_{min} [−]	$p_{\text{FC in}}$ [bar(a)]	$p_{\text{FC out}}$ [bar(a)]	$\mu_{\text{sec H}_2\text{min}}$ [%]
100	0.63	1.40	1.60	1.38	41
75	0.47	1.53	1.48	1.27	34
50	0.31	1.87	1.38	1.18	24
25	0.15	2.70	1.30	1.12	18
11	0.07	5.00	1.26	1.09	44

Fig. 14 Entrainment ratio map for each load point (schematic overview)
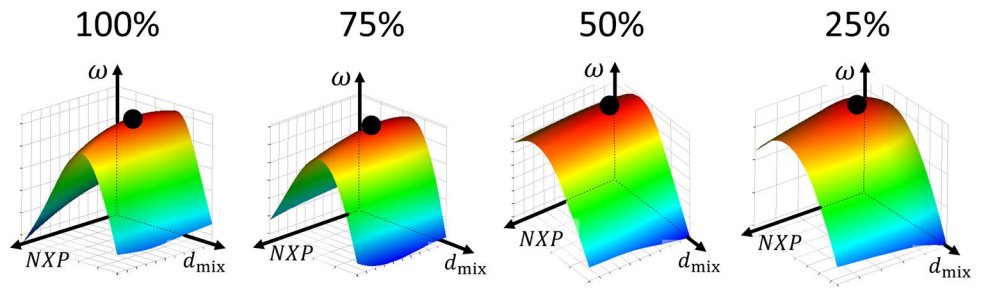
Table 7 Local optima

Load [%]	$d_{\text{mix opt}}$ [mm]	NXP_{opt} [mm]	$l_{\text{mix opt}}$ [mm]	$\lambda_{\text{local opt}}$ [-]
100	6.1	5.0	24	2.52
75	5.3	4.2	22	2.19
50	4.3	3.7	17	1.85
25	3.3	2.9	9	1.40

Table 8 Load map

Load [%]	100	75	50	25	11
Timeshare TS [% of total time]	50	15	15	15	5
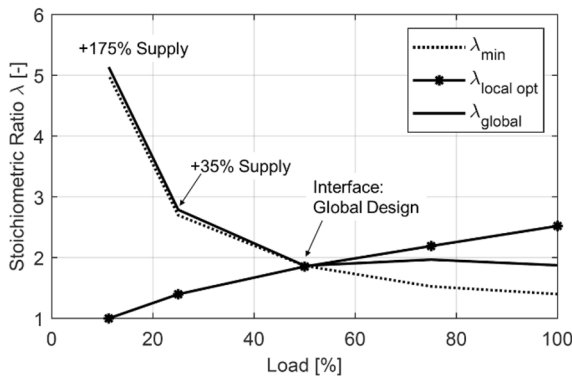
Fig. 15 Stoichiometric ratio

The minimum required stoichiometric ratio for mid-to-high load (50% and above) is achieved. The interface between the local optimum and minimum fuel cell stoichiometric ratio is the global design point which is the geometry at 50% load, since it covers the widest operation range.

Each load point is re-simulated with the global design geometry. The stoichiometric ratio with the global design λ_{global} is lower for high loads but still achieved. However, lower loads need an additional operating strategy to fulfill the minimum required stoichiometric ratio.

First, the number of purge cycles is increased for the 11 and 25% load point, which leads to a higher secondary hydrogen concentration and a higher stoichiometric ratio. However, increased purging is not sufficient and additional hydrogen needs to be supplied by the nozzle to increase nozzle flow impulse and recirculation. The additional hydrogen improves recirculation but is lost by purging. Thus, 35% additional hydrogen must be added for the 25% load point and 175% for the 11% load point. The main

effect on the dynamics of the system is that the purge valve is actuated more frequently or, as a second option, the purge valve is actuated continuously in a partial open state.

The load profile of the PEM FC application needs to be considered to calculate the total hydrogen utilization (Table 8). In total, the hydrogen utilization decreases to 97% by this operating strategy considering the load map in Table 8 (Eq. 10). For this application, the additional hydrogen is acceptable due to the very low operating time for the 11% load point.

Equation 10: Hydrogen utilization

$$H_2\text{Utilization} = \frac{\sum_{i=1}^{5} \text{Load}_i \bullet TS_i \bullet \dot{m}_{\text{prim act i}}}{\sum_{i=1}^{5} \text{Load}_i \bullet TS_i \bullet \dot{m}_{\text{prim i}}}. \tag{10}$$

In case the low-load range (11–25%) has a significantly higher timeshare, other operating strategies can be considered. Each of the following systems has better performance over the entire operating range [17]:

- A second low-load ejector in parallel
- A pulsed injector-ejector unit
- A variable nozzle throat area control ejector.

For this application, Table 9 states the final and most important ejector geometries and Fig. 16 displays the final design of the ejector.

The next development toolchain step is the 3D CFD simulation to improve non-rotational symmetric influences based on detailed packaging considerations (cp. Fig. 1). In this publication, geometry optimization using 3D CFD simulation is not discussed in detail, only general findings.

Generally, the performance of the 3D CFD model is highly dependent on the piping. Experience has shown that if the pressure loss in the piping is low, a small loss of

Table 9 Final ejector geometry

Geometry	Value [mm]
Nozzle throat diameter d_t	1.1
Mixing chamber diameter d_{mix}	4.3
Diffuser outlet diameter d_{diff}	22
Nozzle exit position NXP	4
Mixing chamber length l_{mix}	17
Diffuser length l_{diff}	99
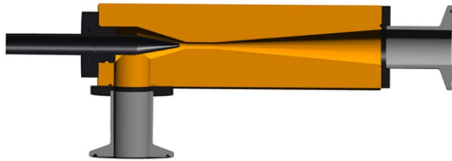
Fig. 16 Ejector CAD

entrainment ratio can be expected ($< 10\%$). In contrast, fillets on each edge within the ejector enhance flow and increase the entrainment ratio in the same range. Thus, if both pipings are added and fillets are applied, the performance will remain approximately in the same entrainment ratio. To minimize the simulation effort, the piping connections to and from the fuel cell and the ejector should be simulated separately using a 3D CFD model. The entire anode path should only be validated using 3D CFD.

4 Conclusion and outlook

The 2D rotational symmetric CFD is explained with a preliminary analysis of the influences on the nozzle hydrogen mass flow, the suction chamber, the mixing chamber, and the diffuser.

The mesh size analysis shows how to minimize computational effort while maintaining high accuracy. A simulation run can take from 3 min to 24 h depending on the mesh size and the necessary accuracy. Furthermore, a smaller mesh size has a lower entrainment ratio, which is a conservative result compared to an extremely high mesh size. By selecting the appropriate mesh size, the simulation time can be reduced by approx. 67% (80 k instead of 200 k), while maintaining high accuracies $< 2\%$.

Maximizing the nozzle inlet temperature and minimizing the secondary temperature increase the entrainment ratio. Impurities, such as nitrogen and water, increase the entrainment ratio but decrease the stoichiometric ratio. Generally, the lower the pressure difference between the ejector outlet and the secondary inlet, the higher the entrainment ratio. The mixing chamber diameter has the biggest influence on performance compared to the nozzle exit position and mixing chamber length.

The ejector geometry should be developed using 2D CFD instead of 3D CFD due to the high computational cost to allow a high number of parameter variations via DoE. The entrainment ratio of the 3D CFD model is dependent on the piping connected between ejector and stack as well as fillets within the ejector. Experience has shown that the piping (additional pressure loss) and the fillet in the ejector (enhanced flow) have an opposite influence on the entrainment ratio and, thus, the entrainment ratio remains in the same range. It is recommended to minimize the pressure losses in the piping in a separate simulation and to use the 3D CFD of the entire anode path only for final validation.

Finally, the ejector design is evaluated from a local analysis to a final ejector design according to the fuel cell stack boundary conditions. A single ejector has a limited operating range, which depends mainly on the nozzle inlet pressure, in this case, 12 bar(a). If an ejector with a larger operating range is required, the nozzle inlet pressure should be increased or other operating concepts, such as a pulsed ejector or a needle ejector, can be used.

Anode recirculation through an ejector instead of a recirculation blower reduces the number of components, weight, moving parts, and power requirements. However, the design of the ejector is critical to maintain the stoichiometric ratio and avoid degradation mechanisms.

This methodology can be applied to a wide range of ejector areas and significantly reduces development efforts in future.

General key findings:

- Maximize nozzle inlet temperature and minimize secondary temperature to maximize entrainment ratio.
- Minimize pressure loss in the anode path and recirculation.
- A small mesh size is a conservative estimation of the entrainment ratio.
- A small mesh size enables a large number of parameter variations over DoE.
- A simple ejector satisfies the stoichiometric ratio in the 50–100% load range for the given fuel cell boundary condition.
- Additional hydrogen is necessary to extend the operating range to lower loads, but results in hydrogen losses.

the project "HyFleet". Both projects form the basis of this publication. The methodological approach was developed in "HyFleet" and the results are taken from the project "HyTechonomy".

Declarations

References

1. Trattner, A., Klell, M., Radner, F.: Sustainable hydrogen society—vision, findings and development of a hydrogen economy using the example of Austria. Int. J. Hydrogen Energy **47**(4), 2059–2079 (2022). https://doi.org/10.1016/j.ijhydene.2021.10.166

2. Klell, M., Eichlseder, H., Trattner, A.: Hydrogen in automotive engineering: production, storage, application. Springer Wiesbaden (2023)

3. Matsumoto, T., Watanabe, N., Sugiura, H., Ishikawa, T.: Development of fuel-cell hybrid vehicle (2001)

4. Tadaichi, M., Nobuo, W., Hiroshi, S., Tetsuhiro, I.: Development of fuel-cell hybrid vehicle. SAE Int. (2002)

5. Yoshikazu, M., Kenji, U.: Development of fuel cell vehicle with next-generation fuel cell stack. SAE Int. (2006)

6. Shinji, A., Mikio, K., Hideaki, M.: Development progress of the toyota fuel cell hybrid vehicle. SAE Int. **2008**, 296–303 (2008)

7. Mikio, K., Hideaki, M., Yasuhiro, N., Tsuyoshi, T., Tadaichi, M., Nobuo, K.: Development of new TOYOTA FCHV-adv fuel cell system. SAE Int. **2009**, 948–954 (2009)

8. Minoru M., Tatsuya F., Kuniaki O.: Advances in the power train system of Honda FCX clarity fuel cell vehicle. SAE Int. (2009)

9. Wang, Y., Chen, K.S., Mishler, J., Cho, S.C., Adroher, X.C.: A review of polymer electrolyte membrane fuel cells: technology, applications, and needs on fundamental research. Appl. Energy **88**(4), 981–1007 (2011). https://doi.org/10.1016/j.apenergy.2010.09.030

10. Konno, N., Mizuno, S., Nakaji, H., Ishikawa, Y.: Development of compact and high-performance fuel cell stack. SAE Int. J. Alt. Power. **4**(1), 123–129 (2015). https://doi.org/10.4271/2015-01-1175

11. Hasegawa, T., Imanishi, H., Nada, M., Ikogi, Y.: Development of the fuel cell system in the mirai FCV. SAE Int. (2016). https://doi.org/10.4271/2016-01-1185

12. Hong, B.K., Kim, S.H.: (Invited) Recent advances in fuel cell electric vehicle technologies of Hyundai. ECS Trans. **86**(13), 3–11 (2018). https://doi.org/10.1149/08613.0003ecst

13. Lohse-Busch, H., Duoba, M., Stutenberg, K., Iliev, S., Kern, M., Richards, B., et al.: Technology assessment of a fuel cell vehicle: 2017 Toyota Mirai. Argonne National Laboratory (2018)

14. Mohrdieck, C., Dehn, S.: Das intelligente brennstoffzellen-plug-in-hybrid-antriebssystem des mercedes-benz GLC F-Cell. ATZ live 2019 (2019)

15. Hong, B.K., Kim, S.H., Kim, C.M.: Powering the future through hydrogen and polymer electrolyte membrane fuel cells. John. Matthey Technol. Rev. (2020). https://doi.org/10.1595/205651319X15744200036826

16. Wang, Y., Ruiz Diaz, D.F., Chen, K.S., Wang, Z., Adroher, X.C.: Materials, technological status, and fundamentals of PEM fuel cells—a review. Mater. Today **32**(7), 178–203 (2020). https://doi.org/10.1016/j.mattod.2019.06.005

17. Singer, G., Gappmayer, G., Macherhammer, M., Pertl, P., Trattner, A.: A development toolchain for a pulsed injector-ejector unit for PEM fuel cell applications. Int. J. Hydrogen Energy **47**(56), 23818–23832 (2022). https://doi.org/10.1016/j.ijhydene.2022.05.177

18. Zhu, Y., Li, Y.: New theoretical model for convergent nozzle ejector in the proton exchange membrane fuel cell system. J. Power Sour. **191**(2), 510–519 (2009). https://doi.org/10.1016/j.jpowsour.2009.02.014

19. Chen, W., Liu, M., Chong, D., Yan, J., Little, A.B., Bartosiewicz, Y.: A 1D model to predict ejector performance at critical and sub-critical operational regimes. Int. J. Refrig **36**(6), 1750–1761 (2013). https://doi.org/10.1016/j.ijrefrig.2013.04.009

20. Dadvar, M., Afshari, E.: Analysis of design parameters in anodic recirculation system based on ejector technology for PEM fuel cells: a new approach in designing. Int. J. Hydrogen Energy **39**(23), 12061–12073 (2014). https://doi.org/10.1016/j.ijhydene.2014.06.046

21. Huang, P.-H., Kuo, J.-K., Wu, C.-B.: Simulation and experimental measurements of 10-kW PEMFC passive hydrogen recovery system. Int. J. Hydrogen Energy **37**, 4457 (2023). https://doi.org/10.1016/j.ijhydene.2023.01.136

22. Kolář, V.D.J.: Verification of K-ω SST turbulence model for supersonic internal flows. International Scholarly and Scientific Research & Innovation, Chicago, New York (2011)

23. Pei, P., Ren, P., Li, Y., Wu, Z., Chen, D., Huang, S., et al.: Numerical studies on wide-operating-range ejector based on anodic pressure drop characteristics in proton exchange membrane fuel cell system. Appl. Energy **235**, 729–738 (2019). https://doi.org/10.1016/j.apenergy.2018.11.005

24. Maghsoodi, A., Afshari, E., Ahmadikia, H.: Optimization of geometric parameters for design a high-performance ejector in the proton exchange membrane fuel cell system using artificial neural network and genetic algorithm. Appl. Therm. Eng. **2014**(1), 410–418 (2014). https://doi.org/10.1016/j.applthermaleng.2014.06.067

25. Liu, Y., Tu, Z., Chan, S.H.: Performance enhancement in a H_2/O_2 PEMFC with dual-ejector recirculation. Int. J. Hydrogen Energy **47**(25), 12698–12710 (2022). https://doi.org/10.1016/j.ijhydene.2022.02.023

26. Liu, Z., Liu, Z., Jiao, K., Yang, Z., Zhou, X., Du, Q.: Numerical investigation of ejector transient characteristics for a 130-kW PEMFC system. Int J Energy Res **44**(5), 3697–3710 (2020). https://doi.org/10.1002/er.5156

27. Nikiforow, K., Koski, P., Karimäki, H., Ihonen, J., Alopaeus, V.: Designing a hydrogen gas ejector for 5 kW stationary PEMFC

system—CFD-modeling and experimental validation. Int. J. Hydrogen Energy **41**(33), 14952–14970 (2016). https://doi.org/10.1016/j.ijhydene.2016.06.122

28. Hosseinzadeh, E., Rokni, M., Jabbari, M., Mortensen, H.: Numerical analysis of transport phenomena for designing of ejector in PEM forklift system. Int. J. Hydrogen Energy **39**(12), 6664–6674 (2014). https://doi.org/10.1016/j.ijhydene.2014.02.061

29. Besagni, G., Mereu, R., Inzoli, F., Chiesa, P.: Application of an integrated lumped parameter-CFD approach to evaluate the ejector-driven anode recirculation in a PEM fuel cell system. Appl. Therm. Eng. **121**, 628–651 (2017). https://doi.org/10.1016/j.applthermaleng.2017.04.111

30. Han, J., Feng, J., Peng, X.: Phase change characteristics and their effect on the performance of hydrogen recirculation ejectors for PEMFC systems. Int. J. Hydrogen Energy **43**, 17857 (2021). https://doi.org/10.1016/j.ijhydene.2021.10.049

31. Xing, L., Shi, W., Su, H., Xu, Q., Das, P.K., Mao, B., et al.: Membrane electrode assemblies for PEM fuel cells: a review of functional graded design and optimization. Energy **177**, 445–464 (2019). https://doi.org/10.1016/j.energy.2019.04.084

32. Elwan, H.A., Mamlouk, M., Scott, K.: A review of proton exchange membranes based on protic ionic liquid/polymer blends for polymer electrolyte membrane fuel cells. J. Power Sour. **484**(2), 229197 (2021). https://doi.org/10.1016/j.jpowsour.2020.229197

33. Ahmad, S., Nawaz, T., Ali, A., Orhan, M.F., Samreen, A., Kannan, A.M.: An overview of proton exchange membranes for fuel cells: materials and manufacturing. Int. J. Hydrogen Energy **47**(44), 19086–19131 (2022). https://doi.org/10.1016/j.ijhydene.2022.04.099

34. Pyoungho, C., Nikhil, J., Ravindra, D.: Thermodynamics and proton transport in nafion: I. membrane swelling, sorption, and ion-exchange equilibrium. J. Electrochem. Soc. (2005). https://doi.org/10.1149/1.1855872

35. Pyoungho, C., Nikhil, J., Ravindra, D.: Thermodynamics and proton transport in nafion: II. Proton diffusion mechanisms and conductivity. J. Electrochem. Soc. (2005). https://doi.org/10.1149/1.1859814.

36. Peighambardoust, S.J., Rowshanzamir, S., Amjadi, M.: Review of the proton exchange membranes for fuel cell applications. Int. J. Hydrogen Energy **35**(17), 9349–9384 (2010). https://doi.org/10.1016/j.ijhydene.2010.05.017

37. Zamel, N.: The catalyst layer and its dimensionality—a look into its ingredients and how to characterize their effects. J. Power Sour. **309**, 141–159 (2016). https://doi.org/10.1016/j.jpowsour.2016.01.091

38. Litster, S., McLean, G.: PEM fuel cell electrodes. J. Power Sour. **130**(1–2), 61–76 (2004). https://doi.org/10.1016/j.jpowsour.2003.12.055

39. Zhou, Y., Lin, G., Shih, A.J., Hu, S.J.: A micro-scale model for predicting contact resistance between bipolar plate and gas diffusion layer in PEM fuel cells. J. Power Sour. **163**(2), 777–783 (2007). https://doi.org/10.1016/j.jpowsour.2006.09.019

40. Lorenzini-Gutierrez, D., Hernandez-Guerrero, A., Ramos-Alvarado, B., Perez-Raya, I., Alatorre-Ordaz, A.: Performance analysis of a proton exchange membrane fuel cell using tree-shaped designs for flow distribution. Int. J. Hydrogen Energy **38**(34), 14750–14763 (2013). https://doi.org/10.1016/j.ijhydene.2013.08.012

41. Lim, J.W., Lee, D.G.: Carbon composite hybrid bipolar plates with bypass-connected gas diffusion layers for PEM fuel cells. Compos. Struct. **95**(2), 557–563 (2013). https://doi.org/10.1016/j.compstruct.2012.08.030

42. Lai, X., Liu, D.A., Peng, L., Ni, J.: A mechanical–electrical finite element method model for predicting contact resistance between bipolar plate and gas diffusion layer in PEM fuel cells. J. Power Sour. **182**(1), 153–159 (2008). https://doi.org/10.1016/j.jpowsour.2008.03.069

43. Iranzo, A., Gregorio, J.M., Boillat, P., Rosa, F.: Bipolar plate research using computational fluid dynamics and neutron radiography for proton exchange membrane fuel cells. Int. J. Hydrogen Energy **45**(22), 12432–12442 (2020). https://doi.org/10.1016/j.ijhydene.2020.02.183

44. Qiu, D., Peng, L., Yi, P., Lehnert, W., Lai, X.: Review on proton exchange membrane fuel cell stack assembly: quality evaluation, assembly method, contact behavior and process design. Renew. Sustain. Energy Rev. **152**, 111660 (2021). https://doi.org/10.1016/j.rser.2021.111660

45. O'Hayre, R.P., Cha, S.-W., Colella, W.G., Prinz, F.B.: Fuel cell fundamentals. Wiley, Hoboken New Jersey (2016)

46. Liu, Y., Xiao, B., Zhao, J., Fan, L., Luo, X., Tu, Z., et al.: Performance degradation of a proton exchange membrane fuel cell with dual ejector-based recirculation. Energy Convers. Manag. X **12**(23), 100114 (2021). https://doi.org/10.1016/j.ecmx.2021.100114

47. Wang, X., Lu, Y., Zhang, B., Liu, J., Xu, S.: Experimental analysis of an ejector for anode recirculation in a 10 kW polymer electrolyte membrane fuel cell system. Int. J. Hydrogen Energy **17**, 794 (2021). https://doi.org/10.1016/j.ijhydene.2021.10.140

48. Liu, Z., Chen, J., Liu, H., Yan, C., Hou, Y., He, Q., et al.: Anode purge management for hydrogen utilization and stack durability improvement of PEM fuel cell systems. Appl. Energy **275**(75), 115110 (2020). https://doi.org/10.1016/j.apenergy.2020.115110

49. Migliardini, F., Di Palma, T.M., Gaele, M.F., Corbo, P.: Hydrogen purge and reactant feeding strategies in self-humidified PEM fuel cell systems. Int. J. Hydrogen Energy **42**(3), 1758–1765 (2017). https://doi.org/10.1016/j.ijhydene.2016.06.196

50. Steinberger, M., Geiling, J., Oechsner, R., Frey, L.: Anode recirculation and purge strategies for PEM fuel cell operation with diluted hydrogen feed gas. Appl. Energy **232**(7), 572–582 (2018). https://doi.org/10.1016/j.apenergy.2018.10.004

51. Aslam, R.M., Ingham, D.B., Ismail, M.S., Hughes, K.J., Ma, L., Pourkashanian, M.: Simultaneous direct visualisation of liquid water in the cathode and anode serpentine flow channels of proton exchange membrane (PEM) fuel cells. J. Energy Inst. **91**(6), 1057–1070 (2018). https://doi.org/10.1016/j.joei.2017.07.003

52. Chen, Z.X., Ingham, D.B., Ismail, M.S., Ma, L., Hughes, K.J., Pourkashanian, M.: Dynamics of liquid water in the anode flow channels of PEM fuel cells: a numerical parametric study. J. Energy Inst. **92**(6), 1956–1967 (2019). https://doi.org/10.1016/j.joei.2018.10.016

53. Wallnöfer-Ogris, E., Pertl, P., Trattner, A.: Quasi-stationary UI-characteristic model of a PEM fuel cell–evaluating the option of self-humidifying operation. Int. J. Hydrogen Energy **45**(56), 32464–32477 (2020). https://doi.org/10.1016/j.ijhydene.2020.08.254

54. Zhang, C., Zhou, W., Zhang, L., Chan, S.H., Wang, Y.: An experimental study on anode water management in high temperature PEM fuel cell. Int. J. Hydrogen Energy **40**(13), 4666–4672 (2015). https://doi.org/10.1016/j.ijhydene.2015.02.037

55. Liu, Z., Yang, L., Mao, Z., Zhuge, W., Zhang, Y., Wang, L.: Behavior of PEMFC in starvation. J. Power Sour. **157**(1), 166–176 (2006). https://doi.org/10.1016/j.jpowsour.2005.08.006

56. Rabbani, A., Rokni, M.: Effect of nitrogen crossover on purging strategy in PEM fuel cell systems. Appl. Energy **111**(1), 1061–1070 (2013). https://doi.org/10.1016/j.apenergy.2013.06.057

57. Baumgartner, W.R., Parz, P., Fraser, S.D., Wallnöfer, E., Hacker, V.: Polarization study of a PEMFC with four reference electrodes at hydrogen starvation conditions. J. Power Sour. **182**(2), 413–421 (2008). https://doi.org/10.1016/j.jpowsour.2008.01.001

58. Maass, S., Finsterwalder, F., Frank, G., Hartmann, R., Merten, C.: Carbon support oxidation in PEM fuel cell cathodes. J. Power Sour. **176**(2), 444–451 (2008). https://doi.org/10.1016/j.jpowsour.2007.08.053

59. Tang, H., Qi, Z., Ramani, M., Elter, J.F.: PEM fuel cell cathode carbon corrosion due to the formation of air/fuel boundary at the anode. J. Power Sour. **158**(2), 1306–1312 (2006). https://doi.org/10.1016/j.jpowsour.2005.10.059

60. Zhao, J., Tu, Z., Chan, S.H.: Carbon corrosion mechanism and mitigation strategies in a proton exchange membrane fuel cell (PEMFC): a review. J. Power Sour. **488**, 229434 (2021). https://doi.org/10.1016/j.jpowsour.2020.229434

61. Jia, F., Guo, L., Liu, H.: Mitigation strategies for hydrogen starvation under dynamic loading in proton exchange membrane fuel cells. Energy Convers. Manage. **139**(1), 175–181 (2017). https://doi.org/10.1016/j.enconman.2017.02.051

62. Nikiforow, K., Koski, P., Ihonen, J.: Discrete ejector control solution design, characterization, and verification in a 5 kW PEMFC system. Int. J. Hydrogen Energy **42**(26), 16760–16772 (2017). https://doi.org/10.1016/j.ijhydene.2017.05.151

63. James, B., Juya-Kouadio, J., Houchins, C.: 2017 DOE Hydrogen and fuel cells program review; project ID# FC163: fuel cell systems analysis. In:Project ID# FC163. [October 15, 2021]; Available at: https://www.hydrogen.energy.gov/pdfs/review17/fc163_james_2017_o.pdf.

64. Toghyani, S., Baniasadi, E., Afshari, E.: Performance analysis and comparative study of an anodic recirculation system based on electrochemical pump in proton exchange membrane fuel cell. Int. J. Hydrogen Energy **43**(42), 19691–19703 (2018). https://doi.org/10.1016/j.ijhydene.2018.08.194

65. Jenssen, D., Berger, O., Krewer, U.: Improved PEM fuel cell system operation with cascaded stack and ejector-based recirculation. Appl. Energy **195**, 324–333 (2017). https://doi.org/10.1016/j.apenergy.2017.03.002

66. Kim, M., Lee, W.-Y., Kim, C.-S.: Development of the variable multi-ejector for a mini-bus PEMFC system. ECS Trans. **5**(1), 773–780 (2007). https://doi.org/10.1149/1.2729058

67. Brunner, D.A., Marcks, S., Bajpai, M., Prasad, A.K., Advani, S.G.: Design and characterization of an electronically controlled variable flow rate ejector for fuel cell applications. Int. J. Hydrogen Energy **37**(5), 4457–4466 (2012). https://doi.org/10.1016/j.ijhydene.2011.11.116

68. Xue, H., Wang, L., Zhang, H., Jia, L., Ren, J.: Design and investigation of multi-nozzle ejector for PEMFC hydrogen recirculation. Int. J. Hydrogen Energy **45**(28), 14500–14516 (2020). https://doi.org/10.1016/j.ijhydene.2020.03.166

69. Du, Z., Liu, Q., Wang, X., Wang, L.: Performance investigation on a coaxial-nozzle ejector for PEMFC hydrogen recirculation system. Int. J. Hydrogen Energy **46**(76), 38026–38039 (2021). https://doi.org/10.1016/j.ijhydene.2021.09.048

70. Liu, Y., Tu, Z., Chan, S.H.: Applications of ejectors in proton exchange membrane fuel cells: a review. Fuel Process. Technol. **214**, 106683 (2021). https://doi.org/10.1016/j.fuproc.2020.106683

71. Song, Y., Wang, X., Wang, L., Pan, F., Chen, W., Xi, F.: A twin-nozzle ejector for hydrogen recirculation in wide power operation of polymer electrolyte membrane fuel cell system. Appl. Energy **300**(1–2), 117442 (2021). https://doi.org/10.1016/j.apenergy.2021.117442

72. Feng, J., Han, J., Hou, T., Peng, X.: Performance analysis and parametric studies on the primary nozzle of ejectors in proton exchange membrane fuel cell systems. Energy Sour. Part A Recov.

Utilizat. Environ. Effects (2020). https://doi.org/10.1080/15567036.2020.1804489

73. Lemmon, E. W., Bell, I. H., Huber, M. L., McLinden, M.O.: NIST standard reference database 23: reference fluid thermodynamic and transport properties-REFPROP, version 10.0. In: National Institute of Standards and Technology (2018). https://doi.org/10.18434/T4/1502528. Available at https://www.nist.gov/srd/refprop

74. Bodo, M., Rainer, K.: Experiences with sonic nozzles used for different gases and wide range of pressure and temperature conditions. In: 7th International Symposium on Fluid Flow Measurement (2009)

75. Bodo, M., Jean-Pierre, V., Chunhui, L., John, W.: Extended data analysis of bilateral comparisons with air and natural gas up to 5 MPA. In: 17th International Flow Measurement Conference (2016)

76. Ishibashi, M.: Discharge coefficient equation for critical-flow toroidal-throat venturi nozzles covering the boundary-layer transition regime. Flow Meas. Instrum. **44**(4), 107–121 (2015). https://doi.org/10.1016/j.flowmeasinst.2014.11.009

77. Measurement of gas flow by means of critical flow nozzles: DIN EN ISO 9300:2021. DIN-Normenausschuss Technische Grundlagen (NATG) (2021)

78. Bodo, M.: Discharge coefficients of CFVN predicted for high Reynolds numbers based on Low-Re-calibration. In: 18th International Flow Measurement Conference (2019)

79. Tang, S.P., Fenn, J.B.: Experimental determination of the discharge coefficients for critical flow through an axisymmetric nozzle. AIAA J. **16**, 41–46 (1978). https://doi.org/10.2514/3.60854

80. Ma, T., Yang, Y., Lin, W., Yang, Y., Jia, W., Zhang, J.: Design of a novel high-efficiency water separator for proton exchange membrane fuel cell system. Int. J. Hydrogen Energy **44**(11), 5462–5469 (2019). https://doi.org/10.1016/j.ijhydene.2018.10.109

81. Han, J., Feng, J., Hou, T., Chen, W., Peng, X.: Numerical and experimental study on gas-water separators for a PEMFC system. Int. J. Green Energy **18**(5), 490–502 (2021). https://doi.org/10.1080/15435075.2020.1865370

82. Han, J., Feng, J., Chen, P., Liu, Y., Peng, X.: A review of key components of hydrogen recirculation subsystem for fuel cell vehicles. Energy Convers. Manag. X **15**(7867), 100265 (2022). https://doi.org/10.1016/j.ecmx.2022.100265

83. Kuo, J.-K., Hsieh, C.-Y.: Numerical investigation into effects of ejector geometry and operating conditions on hydrogen recirculation ratio in 80 kW PEM fuel cell system. Energy **233**, 121100 (2021). https://doi.org/10.1016/j.energy.2021.121100

84. Yang, Y., Du, W., Ma, T., Lin, W., Cong, M., Yang, H., et al.: Numerical studies on ejector structure optimization and performance prediction based on a novel pressure drop model for proton exchange membrane fuel cell anode. Int. J. Hydrogen Energy **45**(43), 23343–23352 (2020). https://doi.org/10.1016/j.ijhydene.2020.06.068

Publisher's Note Springer Nature remains neutral with regard to jurisdictional claims in published maps and institutional affiliations.